In-situ irradiation creep experiment in a TEM revealing fast dislocation glide induced by irradiation in pure copper

Authors: Nargisse Khiara[(1)], Fabien Onimus[(1)], Stéphanie Jublot-Leclerc[(2)], Thomas Jourdan[(3)], Thomas Pardoen[(4)], Jean-Pierre Raskin[(5)], Yves Bréchet[(6)]

[(1)] Université Paris-Saclay, CEA, Service de Recherches Métallurgiques Appliquées, 91191, Gif-sur-Yvette, France
[(2)] Université Paris-Saclay, CNRS/IN2P3, IJCLab, 91405 Orsay, France
[(3)] Université Paris-Saclay, CEA, Service de Recherches de Métallurgie Physique, 91191, Gif-sur-Yvette, France
[(4)] Institute of Mechanics, Materials and Civil Engineering, UCLouvain, Place Sainte Barbe 2 L5.02.02, 1348, Louvain-la-Neuve, Belgium
[(5)] Institute of Information and Communication Technologies, Electronics and Applied Mathematics, UCLouvain, Place du Levant 2 L5.04.04, 1348, Louvain-la-Neuve, Belgium
[(6)] Science et Ingénierie des Matériaux et Procédés (SIMAP), Université Grenoble Alpes, 1130 rue de la Piscine BP 75, 38402, Saint Martin d'Hères, France

Supplementary Data

1. Details on the determination of the activated slip system

The crystallographic orientation of the studied grain was determined using electron diffraction patterns. Usually the slip plane is determined based on stereographic projections and on traces left by dislocations on the thin foil surfaces. However, since the traces were not visible, the dislocation motions were used instead.

First dislocation type (in grey)
Based on the stereographic projection and the orientation of the dislocation pile-up, the glide system seems to either be $(\bar{1}1\bar{1})$ or $(1\bar{1}\bar{1})$ (respectively in blue and green in Figure 1). To find out the actual glide system, we calculate the foil thickness e for the two configurations.

The apparent distance between slip traces d_{app} and the thickness t are linked by the following relation:

$$t = d_{app}\frac{\sin(\theta_0)}{\cos(\theta)} \tag{1.1}$$

with

- θ_0: the angle between the normal to the slip plane and the beam at zero tilt;
- θ: the angle between the normal to the slip plane and the beam at the tilt in which the image was taken.

Both angles can be measured using the software Carine Crystallography. The results presented in Table 1 show that the plane that gives a consistent foil thickness is $(1\bar{1}\bar{1})$ (in green in Figure 1) since a thickness of 29 nm is not possible for such image.

Table 1 – Estimation of the specimen thickness using the two possible planes $(\bar{1}1\bar{1})$ and $(1\bar{1}\bar{1})$.

Plane	$\boldsymbol{\theta}$	$\boldsymbol{\theta_0}$	$\boldsymbol{t}$
$(\bar{\mathbf{1}}\mathbf{1}\bar{\mathbf{1}})$	38°	52°	29 nm (not ok)
$(\mathbf{1}\bar{\mathbf{1}}\bar{\mathbf{1}})$	76°	57°	100 nm (ok)

There are three possible Burgers vectors (grey arrows in Figure 1): $[110]$, $[01\bar{1}]$ and $[\bar{1}0\bar{1}]$.

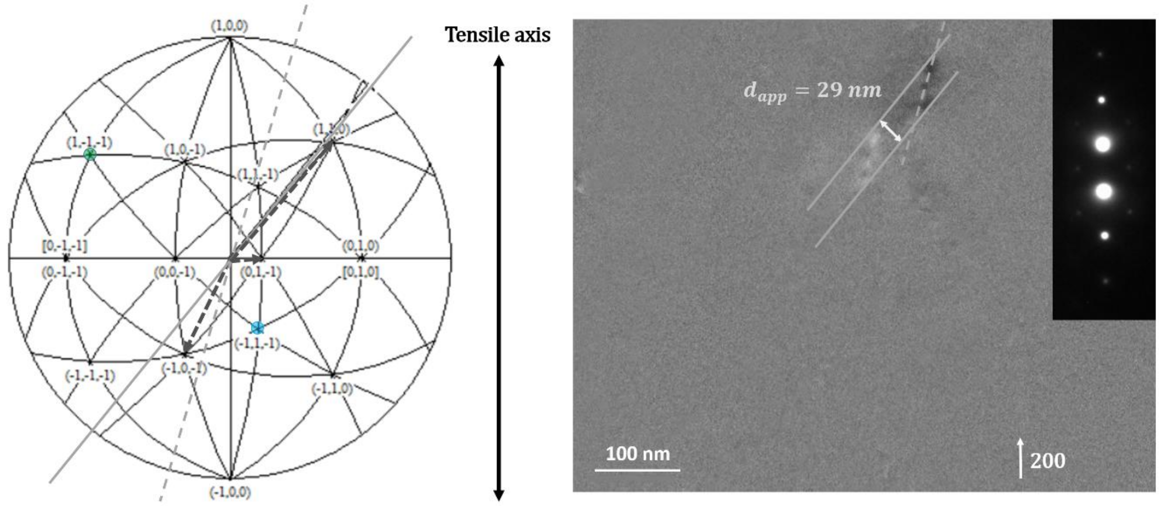

Figure 1 – Determination of the slip system for the first dislocation type.

Given that the tensile axis very close to the axis $[100]$, the glide of the dislocations with a Burgers vector $[01\bar{1}]$ is not activated, the Schmid factor relative to the directions $[110]$ and $[\bar{1}0\bar{1}]$ can be calculated using

$$m = \cos(\gamma)\cos(\chi) \tag{1.2}$$

with

- γ: the angle between the normal to the glide plane and the tensile axis;
- χ: the angle between the glide direction and the tensile axis.

The two directions $[110]$ and $[\bar{1}0\bar{1}]$ have the same Schmid factor equal to 0.409, they can be both equally activated.

Second dislocation type (in red)

The results presented in Table 2 show that the plane that gives a consistent foil thickness is $(11\bar{1})$ (in green in Figure 2). A thickness of 291 nm is not consistent with the image quality. The thickness estimated here (84 nm) is in relatively good agreement with the previously estimated thickness.

Table 2 – Estimation of the specimen thickness using the two possible planes $(\bar{1}1\bar{1})$ and $(11\bar{1})$.

Plane	$\boldsymbol{\theta}$	$\boldsymbol{\theta_0}$	$\boldsymbol{e}$
$(\bar{\mathbf{1}}\mathbf{1}\bar{\mathbf{1}})$	76°	57°	291 nm (not ok)
$(\mathbf{11}\bar{\mathbf{1}})$	38°	52°	84 nm (ok)

There are three possible Burgers vectors (represented by the red arrows in Figure 2): $[0\bar{1}\bar{1}]$, $[\bar{1}0\bar{1}]$ and $[\bar{1}10]$. Given that the tensile axis is very close to the axis $[100]$, the glide of the dislocations with a Burgers vector $[0\bar{1}\bar{1}]$ is not activated. The two directions $[\bar{1}0\bar{1}]$ and $[\bar{1}10]$ have a same Schmid factor equal to 0.409, they can be both equally activated.

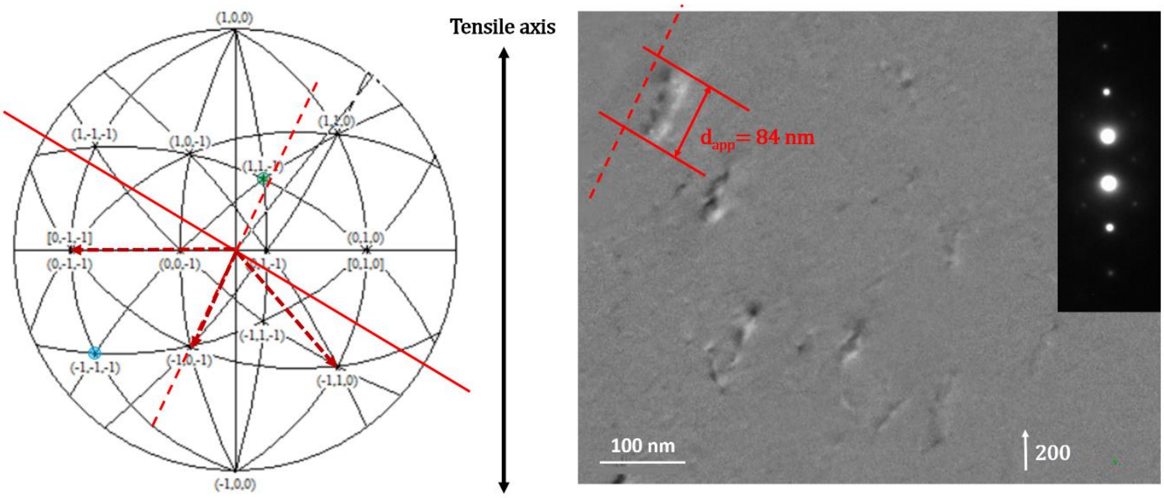

Figure 2 – Determination of the slip system for the second dislocation type.

Third dislocation type (in orange)

The results presented in Table 3 show that the plane that gives a consistent foil thickness is $(\bar{1}1\bar{1})$ (in blue in Figure 3). Again, a thickness of 250 nm is not consistent with the image quality. The thickness estimated (72 nm) here is in good agreement with the previously estimated thicknesses.

Table 3 – Estimation of the specimen thickness using the two possible planes $(\bar{1}1\bar{1})$ and $(1\bar{1}\bar{1})$.

Plane	$\boldsymbol{\theta}$	$\boldsymbol{\theta_0}$	$\boldsymbol{e}$
$(\bar{1}1\bar{1})$	38°	52°	72 nm (ok)
$(1\bar{1}\bar{1})$	76°	57°	250 nm (not ok)

There are three possible Burgers vectors (represented by the yellow arrows in Figure 3): $[110]$, $[\bar{1}01]$ and $[011]$. Given that the tensile axis is the axis $[100]$, the glide of the dislocations with a Burgers vector $[011]$ is not activated. The two directions $[110]$ and $[\bar{1}01]$ have a same Schmid factor equal to 0.409, they can be both equally activated.

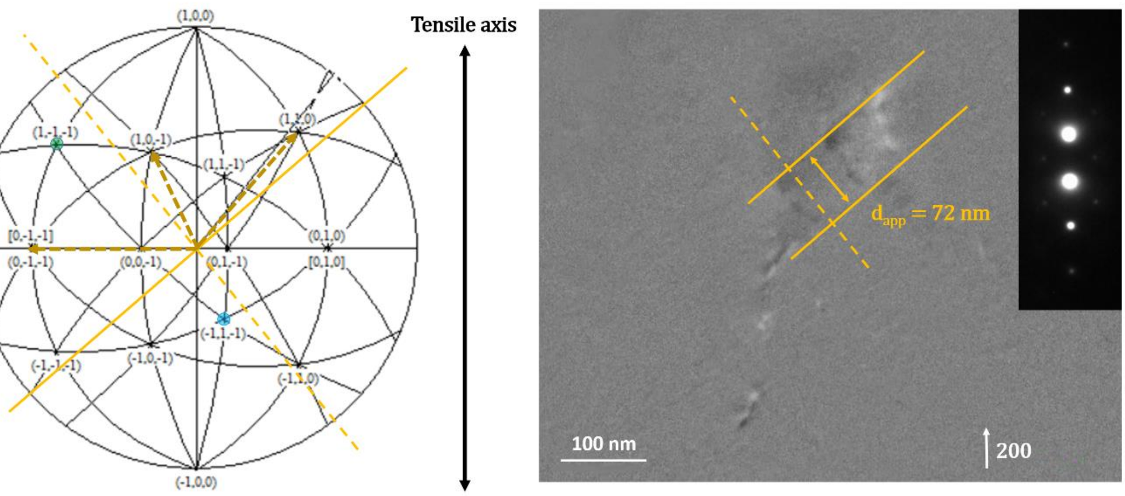

Figure 3 – Determination of the slip system for the third dislocation type.

Cross-slip between the first and second dislocation types

Figure 4 shows a dislocation that glides initially in the plane $(1\bar{1}\bar{1})$ (Figure 4.a-c), then aligns along its screw direction (Figure 4.e-f) to then cross-slip in the plane $(11\bar{1})$ (Figure 4.i-k). Thus, a cross slip event is observed between the dislocations of the $(1\bar{1}\bar{1})$ glide plane and $(11\bar{1})$ glide plane (i.e. between the grey and red dislocation types). This shows that the dislocations of those two families are screw dislocations. Therefore, their Burgers vector can be determined as $[\bar{1}0\bar{1}]$. This is consistent with the alignment of the dislocations along this direction.

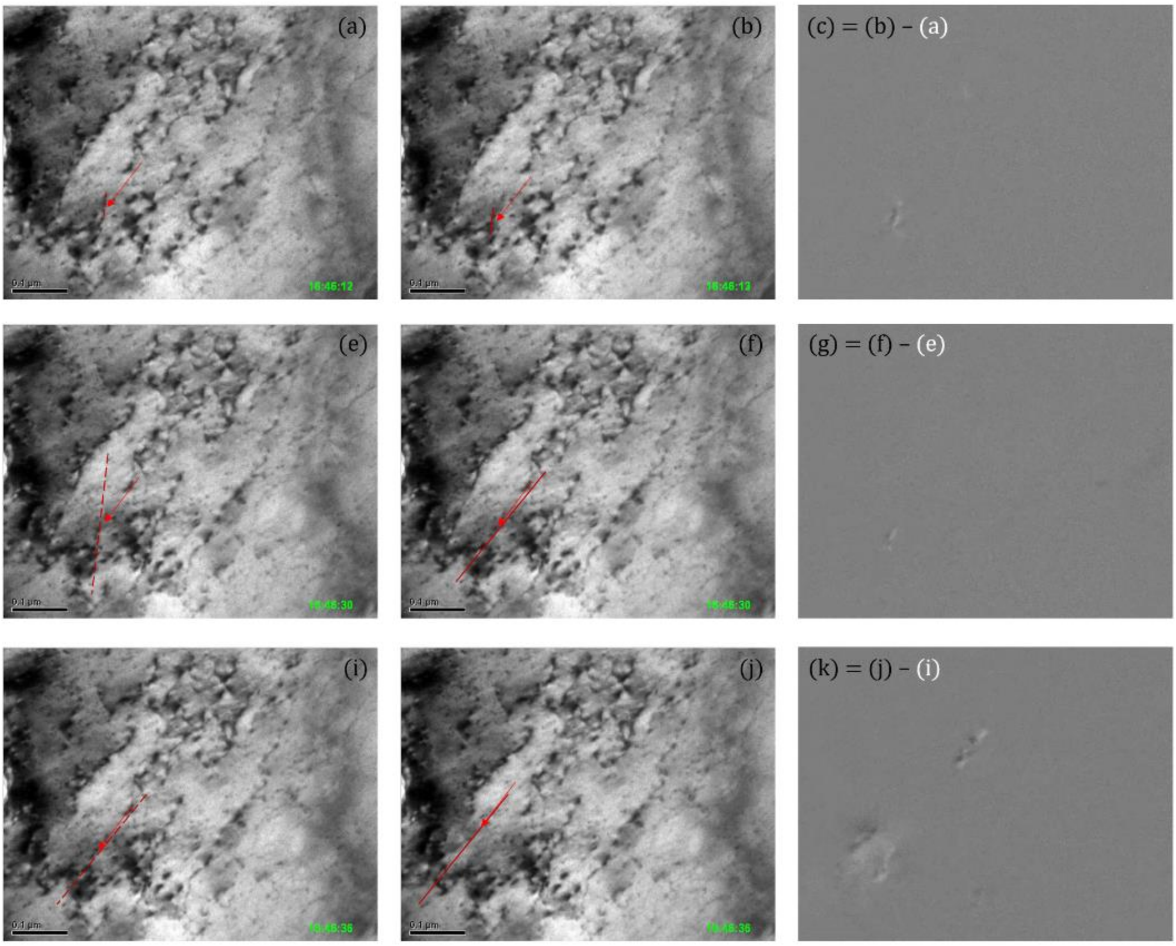

Figure 4 – Cross-slip observed between the first and second dislocation type.

V-shaped dislocations

V-shaped dislocations are observed during the experiments. The crystallographic orientation of the grain is determined using electron diffraction. As shown in Figure 5, the tip of the V shape moves along the $[110]$ axis. Moreover, the dislocations are invisible for the following diffraction vectors: $[1\bar{1}\bar{3}]$, $[\bar{1}1\bar{1}]$, $[\bar{1}1\bar{3}]$ and $[002]$, which is consistent with a Burgers vector $\frac{1}{2}[110]$. In addition, as shown in green and red in Figure 5, the traces of the two segments of each dislocation correspond to the glide planes $(1\bar{1}1)$ and $(\bar{1}11)$. This indicates that segments of the dislocations have cross-slipped between the planes $(1\bar{1}1)$ and $(\bar{1}11)$.

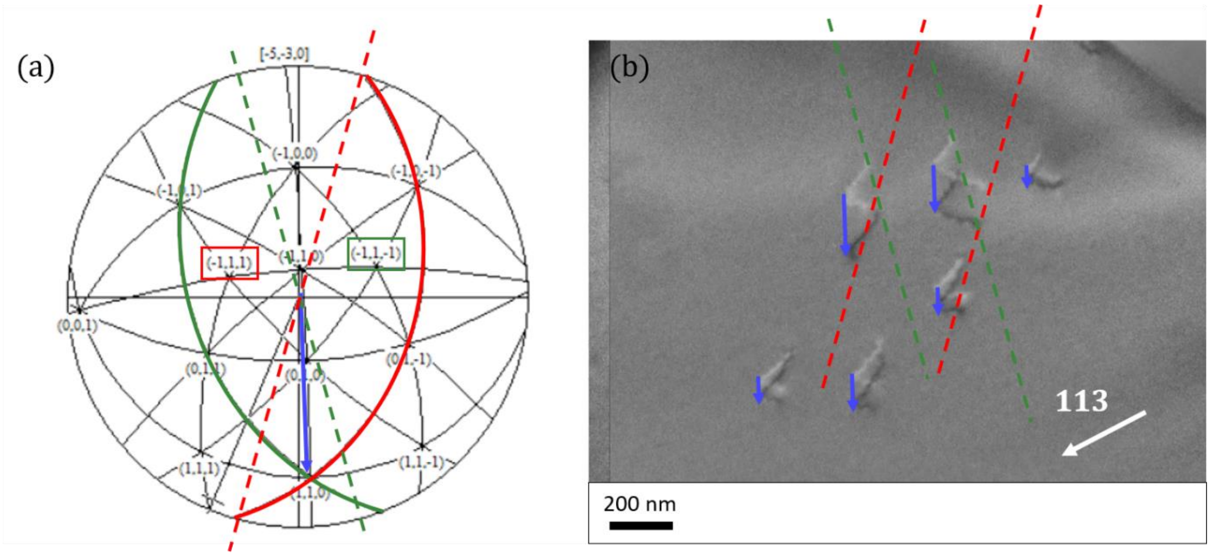

Figure 5 – (a) Stereographic projection – (b) TEM micrograph showing that the tip of the V moves along the [110] axis and that the traces of the islocations are consistent with the glide planes $(1\bar{1}1)$ *and* $(\bar{1}11)$. .

2. Geometrical transformation of the TEM images

The glide plane is often not the image plane. Thus, in order to measure accurate distances in the image, a geometrical transformation is needed. Using the software Carine Crystallography, the rotation angles that permit to go from the glide plane to the image plane can be measured. For instance, for the glide plane $(\bar{1}1\bar{1})$, first a rotation along the Z-axis of -157° is needed, followed by a rotation along the X-axis of 38°. The stereographic images after each rotation are shown in Figure 6. To replicate these transformations on the TEM images, as represented in Figure 6, they are first rotated along the Z-axis with an angle of 157°, then there are rescaled along the X-axis with a magnification of 1/cos(38°). These geometrical transformations were performed using the tool TransformJ in the image processing program Fiji [1].

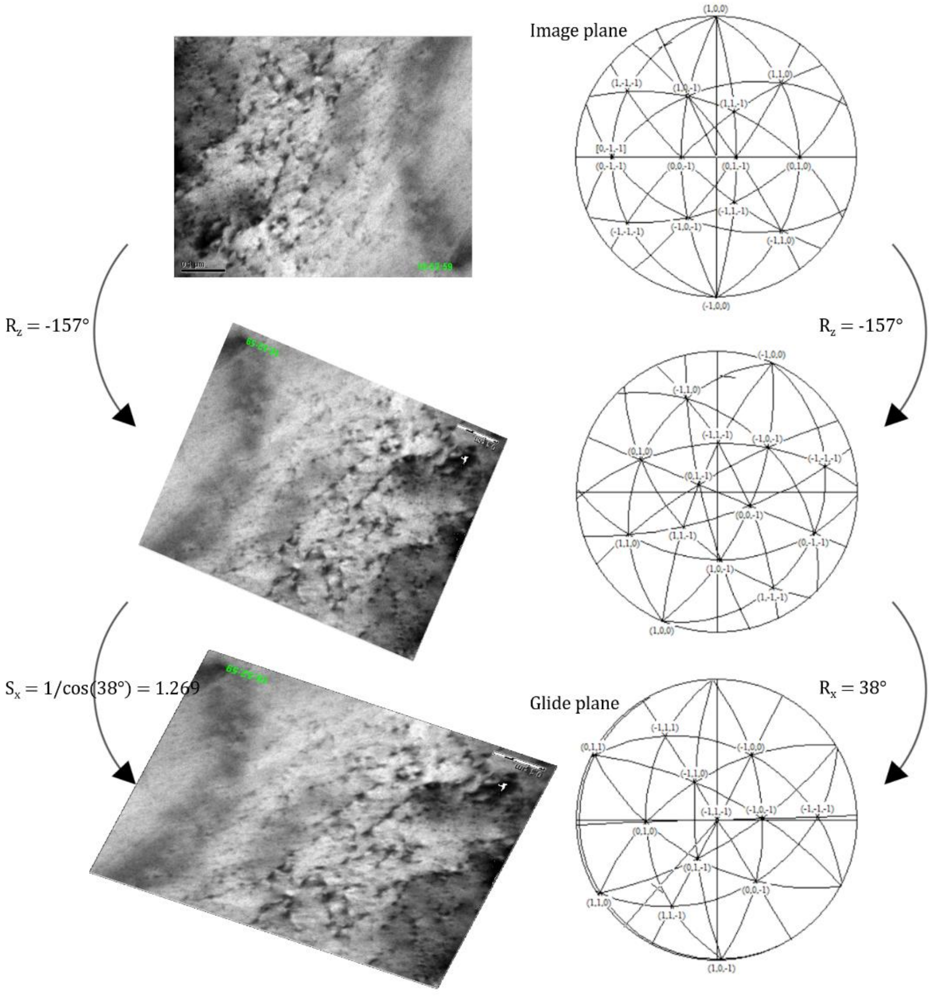

Figure 6 – Geometrical transformation to project the image plane into the glide plane.

3. Potential effect of ion beam heating

In order to prove that the unpinning event from irradiation defects is indeed triggered by irradiation and does not result from ion beam heating effects, an estimation of the specimen heating during ion irradiation is computed. The specimen is modelled as a rectangle of 11 mm x 2.3 mm and of thickness 0.13 mm maintained at its ends by the straining holder. The irradiated area in the middle of the sample is a disk of 1.5 mm diameter (S_{irr}^{ions}= 7.1 mm²). Assuming, in extreme case, that all the kinetic energy of the ion (E = 2 MeV) is lost in the sample, and knowing the ion flux (φ = $1.2.10^{10}$ ions/cm²/s to φ = 1.10^{11} ions/cm²/s) the maximum value for the deposited power on the irradiated surface can be calculated using:

$$P^{ions} = E\varphi S_{irr}^{ions} \tag{3.1}$$

The cross-heads of the holder are considered as the heat sinks because of their large volume compared to the sample and have a constant temperature with or without the ion beam. The heat flux towards one of the two cross-heads, in the steady state regime, corresponds to half of the power deposited on the irradiated surface (i.e. $P^{ions}/2$).

Knowing the sample cross section (S_0 = 0.299 mm²), the distance to the cold sink (L_D = 5 mm) and the thermal conductivity of copper (κ = 401 W/m/K), the heat flux Q toward the cross-heads can be related to the increase in temperature ΔT using:

$$Q = \frac{\kappa \times \Delta T \times S_0}{L_D}. \tag{3.2}$$

Therefore, the increase in temperature is:

$$\Delta T = \frac{E\varphi S_{irr}^{ions}}{2}\frac{L_D}{\kappa S_0} = 0.006\,K \text{ to } 0.05\,K. \tag{3.3}$$

Two extra experiments have been performed to further compare the effect of the ion beam heating to the electron beam heating on an unirradiated specimen (first experiment) and a previously irradiated specimen (second experiment). A 200 keV electron irradiation, unlike a 2 MeV Cu^+ ion irradiation, does not induce lattice damage in copper [3]. Therefore, the energy loss within the copper specimen due to the electron irradiation is only dissipated as heat, whereas for the ion irradiation, the energy loss is dissipated as heat and lattice damage (displacement cascades, irradiation defects).

The first experiment, reported in Figure 7, is performed on an unirradiated specimen. Therefore, in this case, the dislocations are not pinned on irradiation defects. At first (Figure 7.a and Figure 7.e), the electron beam is not focused and no dislocation motion is observed, then the electron beam is focused on dislocations during a couple of seconds (Figure 7.b and Figure 7.f) and the dislocations start to glide. The electron beam is, again, defocused and no dislocation motion is observed (Figure 7.c and Figure 7.g). Finally, the ion beam is turned on for 60 seconds (it is the first irradiation step) and no motion of the dislocations is observed (Figure 7.d and Figure 7.h). This shows that the heating induced by the focused electron beam is larger than the heating due to the ion beam. This experiment has been reproduced several times with the same outcome.

The second experiment is performed on a pre-irradiated specimen (Figure 8). The electron beam is focused, during a couple of seconds, on dislocations pinned on irradiation defects and no dislocation motion is observed (Figure 8.a and Figure 8.g). Then, the electron beam is defocused with no dislocation motion again (Figure 8.b and Figure 8.h). The ion beam is then turned on and dislocation motions are observed. This shows that the heating due to the focused electron beam was not sufficient to induce the unpinning of dislocations. Thus, since the ion beam heating is lower than the electron beam heating, the dislocation motion observed during this second experiment does not result from heating effects.

In the conditions of the experiments detailed in Figure 7 and Figure 8, the power deposited by the ion beam per unit of area (P^{ions}/S_{irr}^{ions}) is of 1.60×10^2 W/m². Moreover, the power per surface area absorbed by the specimen due to the electron beam can be estimated from the average rate of the energy lost in the specimen by the electron beam calculated using the Bethe-Bloch expression [2]:

$$-\frac{\mathrm{d}E}{\mathrm{d}z} = \frac{2\pi Z\rho(e^2/4\pi\varepsilon_0)^2}{mv^2}\left\{\ln\left[\frac{E(E+mc^2)^2\beta^2}{2{I_e}^2mc^2}\right] + (1+\beta^2) - \left(2-\sqrt{1-\beta^2}-1+\beta^2\right)\ln 2 + \frac{1}{8}\left(1-\sqrt{1-\beta^2}\right)^2\right\}$$

With:

- $Z = 29$: atomic number of the target element
- $\rho = 4.271 \times 10^{28}$ at/m³: the density
- e: charge of the electron

- ε_0: dielectric constant
- m: mass of the electron
- $\beta = v/c$
- $E = 200$ keV: beam energy
- c: speed of the light in a vacuum
- $I_e = 322$ eV: mean excitation energy

Knowing the thickness of the specimen t and the electron dose rate r (in electrons/m²/s), the surface power lost in the specimen by the electron beam is:

$$P_S^{electrons} = \left(-\frac{\mathrm{d}E}{\mathrm{d}z}\right) \times t \times r \tag{4.1}$$

The surface power lost in the specimen calculated in the different configurations presented in the article are listed in Table 4.

Table 4 – Surface power lost in the specimen for the different configurations considered in the manuscript.

	De-focused electron beam	Focused electron beam
Figure 7	2.50×10^5 W/m²	1.93×10^6 W/m²
Figure 8	4.32×10^5 W/m²	8.18×10^6 W/m²

The value obtained for the de-focused electron beam is three orders of magnitude higher than the impinging power of the ion beam. As stated earlier, the energy loss within the copper specimen due to the electron irradiation is only dissipated as heat, whereas for the ion irradiation, the energy loss is dissipated as heat and lattice damage. Therefore, the heating due to the ion beam is negligible compared with the heating due to the electron beam. These calculations indicate that the ion irradiation induced dislocation motion is not due to ion beam heating effects, but rather due to lattice damage effects.

Moreover, the surface power absorbed by the specimen due to the focused electron beam is found around 10^6 W/m² for both experiments, which is one order of magnitude higher than for the defocused electron beam and four orders of magnitude higher than for the ion beam. These observations further consolidate that the phenomenon under investigation here is indeed due to irradiation effects through lattice damage and does not result from ion beam heating effects.

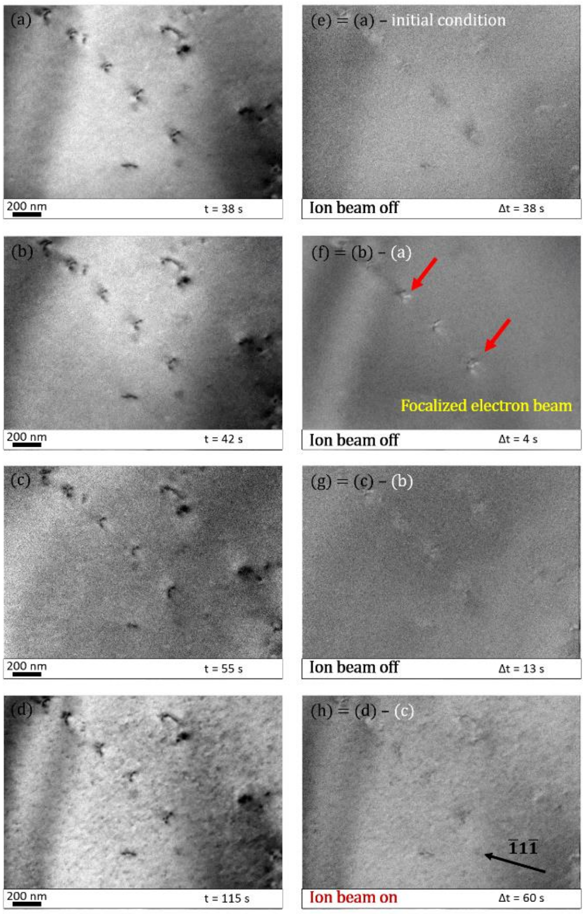

Figure 7 – TEM micrographs for an unirradiated specimen at the end of different steps: (a) 38 seconds of pause, (b) electron beam focus of few seconds, (c) 13 seconds of pause before ion irradiation, (d) the first ion irradiation step. Image subtractions during each phase in the same order: (e), (f), (g) and h. The red arrows point at the moving dislocations. Bright Field TEM, g = $\bar{1}1\bar{1}$*, close to zone axis* $[\bar{1}12]$*. The crosshead displacement is held constant (δ = 152 µm).*

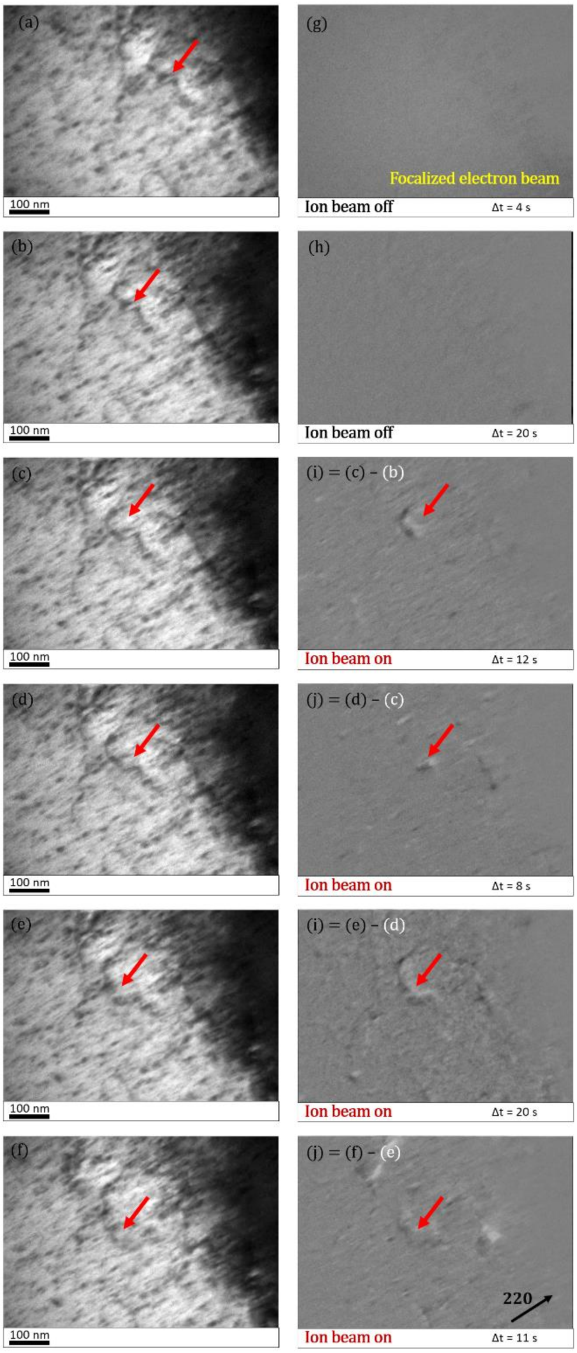

Figure 8 – TEM micrographs for a previously irradiated specimen at the end of different steps: (a) few seconds of electron beam focusing, (b) 20 seconds of pause, (c)-(f) during an ion beam irradiation. Image subtractions corresponding to each step in the same order: (g)-(j). The red arrows point at a moving dislocation. Bright Field TEM, g = 220, close to zone axis $[00\bar{1}]$. *The crosshead displacement is held constant (δ = 157 µm).*

4. Rate theory calculations

In the following, the climb velocity and climb duration is estimated for the three classical climb and glide creep mechanisms in the conditions of our experiments (dislocation density around 10^{13} m^{-2} and stress around 150 MPa).

Model assumptions

The first climb induced irradiation creep mechanism considered here is the climb driven by the so-called dislocation bias mechanism. It results from a stronger elastic interaction between edge dislocations and interstitials than between edge dislocations and vacancies. This leads to a net absorption of interstitials by edge dislocations, provided that there is an equivalent absorption of vacancies by other sinks. Given the thinness of the sample (around 100 nm), we consider the other sinks, beside the edge dislocations, to be the foil surfaces.

However, for climb and glide due to dislocation bias, the climb velocity does not depend on the applied stress, whereas the mechanism observed experimentally is highly stress dependent. There are other mechanisms that can explain the climb of edge dislocations for which the climb velocity increases with increasing stress. These are referred to as stress-induced preferential absorption of point defects (SIPA) mechanisms. Two main SIPA models are found in the literature: the SIPA-I (for Stress Induced Preferential Absorption due to Inhomogeneity effects) which results from polarizability effects [4, 5], and the SIPA-AD (for Stress Induced Preferential Absorption due to Anisotropic Diffusion) which is due to elastodiffusion and is considered to be a first order effect [6].

Therefore, in our calculations, we consider two types of sinks: the thin film surfaces and edge dislocations uniformly distributed through the foil. The latter are subdivided into N classes. Each class n, of line density ρ_n has a Burgers vector $\boldsymbol{b_n}$ making an angle φ_n with the stress, and a line direction making an angle θ_n with the stress.

The parameters for pure copper used for the different computations are given in Table 5.

Table 5 – Computation parameters for pure copper

Parameter	**Symbol**	**Value or definition**
Atomic volume	Ω	1.18×10^{-29} m^3
Lattice parameter	a_0	3.6147×10^{-10} m
Burgers vector	b	2.56×10^{-10} m
Elastic constants (Experimental results from Ref. [7, 8])	C_{11}	176 GPa
	C_{12}	123 GPa
	C_{44}	81.7 GPa
Elastic polarizability for self-interstitials [9]	$\frac{1}{x_i}\frac{\Delta C_{44}^i}{C_{44}}$	-17 ± 2
	$\frac{1}{x_i}\frac{\Delta c_i{}'}{c'}$	-16 ± 2
	$\frac{1}{x_i}\frac{\Delta \kappa_i}{\kappa}$	-2 ± 2
Recombination radius	r_{iv}	$3a_0$

Migration energy for interstitials [10]	ΔH_m^i	0.12 eV
Migration energy for vacancies [10]	ΔH_m^v	0.7 eV
Factor for the diffusion coefficient of interstitials	a_i	$2/3$
Factor for the diffusion coefficient of vacancies	a_v	1
Temperature	T	293 K
Dose rate	D	0.0004 dpa/s
Efficiency coefficient	η	0.2
Elastic dipole tensor for interstitials at the ground state derived from first principles (orientation along [100]) [11]	$\boldsymbol{P}_i^{GS}$	$\begin{bmatrix} 17.46 & 0 & 0 \\ 0 & 17.66 & 0 \\ 0 & 0 & 17.66 \end{bmatrix}$ (in eV)
Elastic dipole tensor for interstitials at the saddle point derived from first principles (jump in the [110] direction) [11]	$\boldsymbol{P}_i^{SP}$	$\begin{bmatrix} 18.01 & 1.78 & 0 \\ 1.78 & 18.01 & 0 \\ 0 & 0 & 18.46 \end{bmatrix}$ (in eV)
Elastic dipole tensor for vacancies at the ground state derived from first principles [11]	$\boldsymbol{P}_v^{GS}$	$\begin{bmatrix} -3.19 & 0 & 0 \\ 0 & -3.19 & 0 \\ 0 & 0 & -3.19 \end{bmatrix}$ (in eV)
Elastic dipole tensor for vacancies at the saddle point derived from first principles (jump in the [110] direction) [11]	$\boldsymbol{P}_v^{SP}$	$\begin{bmatrix} -3.61 & -0.37 & 0 \\ -0.37 & -3.61 & 0 \\ 0 & 0 & 2.12 \end{bmatrix}$ (in eV)

Expressions for the climb velocities and pinning lifetimes

The climb velocity v_n of a dislocation in the n^{th} class is given by [12]:

$$v_n = \frac{1}{b}(z_i^n D_i C_i - z_v^n D_v C_v). \tag{4.1}$$

In this equation C_j is the atomic fraction of point defect j (the subscripts i and v refer to interstitials and vacancies, respectively), D_j is the diffusion coefficient of the point defect j, z_j^n is the absorption efficiency of the dislocations of the n^{th} class with respect to point defect j, and b is the norm of the Burgers vector ($b = b_n = |\boldsymbol{b_n}|$).

The upper bound for climb velocity is:

$$v_c = \max_n |v_n|\,. \tag{4.2}$$

In the case of climb driven by dislocation bias, all the dislocations are equivalent (i.e. $v_n = v$). For the two SIPA mechanisms, we make the hypothesis, usually assumed for isotropic cubic materials, that there are three classes of dislocations (i.e. $N = 3$). One third of the dislocations are “aligned” (i.e. $\varphi_1 = 0$ for SIPA-I and $\theta_1 = 0$ for SIPA-AD), and the other two thirds are “not-aligned” (i.e. $\varphi_2 = \varphi_3 = \pi/2$ for SIPA-I and $\theta_2 = \theta_3 = \pi/2$ for SIPA-AD). Dislocations with different orientations have different values of z_j^n which depend on the stress σ, so their climb velocities also differ.

Considering an obstacle height h of 1 nm (half loop size), the pinning lifetime can be evaluated as:

$$\tau = \frac{h}{v_c}. \tag{4.3}$$

The point defects concentrations can be calculated using the rate theory in the steady state regime [4, 6, 12]:

$$C_j = aK_0/k_j^2 D_j \,, \tag{4.4}$$

with:

$$a = 2\xi^{-1}\left[(1+\xi)^{1/2} - 1\right], \tag{4.5}$$

$$\xi = 4K_{iv}K_0/D_i\, D_v k_i^2 k_v^2 \,, \tag{4.6}$$

where k_j^2 is the total sink strength for the point defect j, K_0 is the defect production rate and K_{iv} is the recombination rate.

The diffusion coefficients D_j for vacancies and interstitials can be calculated (neglecting the entropy terms) using [12]:

$$D_j = a_j \times {a_0}^2 \times f \times e^{-\Delta H_m^j / k_B T} \,, \tag{4.7}$$

where ΔH_m^j is the migration energy for the point defect j, f is the Debye frequency (10^{13} s^{-1}), k_B is the Boltzmann constant, T is the temperature, a_0 is the lattice parameter at temperature T, and a_j is a factor which depends on the number of possible jumps for the point defect j towards neighbor positions.

The defect production rate K_0 is related to the damage rate D through an efficiency coefficient η [12]:

$$K_0 = \eta D \,. \tag{4.8}$$

The recombination rate K_{iv} can be estimated as follows [12]:

$$K_{iv} = \frac{4\pi r_{iv}(D_i + D_v)}{\Omega} \approx \frac{4\pi r_{iv} D_i}{\Omega} \,, \tag{4.9}$$

where Ω is the atomic volume and r_{iv} is defined by $r_{iv} = 3a_0$.

The total sink strength k_j^2 is then given by:

$$k_j^2 = k_{j,d}^2 + k_{j,s}^2 \,, \tag{4.10}$$

where $k_{j,s}^2$ is the foil surface sink strength [13], and $k_{j,d}^2$ is the dislocation sink strength depending on the nature of the climb and glide creep mechanisms [4, 6, 12]. Since $k_{j,d}^2$ depends on stress, k_j^2 depends on stress. The expressions for the sink strengths $k_{j,d}^2$ (for the three mechanisms) and $k_{j,s}^2$ are presented in the following paragraphs.

<u>Dislocation sink strength in the case of climb driven by dislocation bias</u>

The dislocation sink strength in the case of climb driven by dislocation bias can be written as follows [12]:

$$k_{j,d}^2 = \rho_D z_j^0 \,, \tag{4.11}$$

where ρ_D is the dislocation density, and z_j^0 is the capture efficiency of dislocations for the point defect j defined by:

$$z_j^0 = \frac{2\pi}{ln\left(4R_d/\left|L_j^0\right|e^{\gamma}\right)} \,, \tag{4.12}$$

$$L_j^0 = \frac{\mu b(1+\nu)}{3(1-\nu)\pi k_B T} \Delta V_j \,, \tag{4.13}$$

with $R_d = (\pi \rho_D)^{-1/2}$, ν the Poisson ratio of copper, $\mu = (C_{11} - C_{12} + 3C_{44})/5$ the shear modulus of copper, C_{ij} the elastic constants of copper, γ the Euler constant, and ΔV_j the relaxation volume of the point defect j which can be derived from the elastic dipole tensor for the point defect at ground state $\boldsymbol{P}_j^{GS}$ using:

$$\Delta V_j = \frac{tr(\boldsymbol{P}_j^{GS})}{3\kappa}, \tag{4.14}$$

where $\kappa = (C_{11} + 2C_{12})/3$ is the bulk modulus.

<u>Dislocation sink strength in the case of SIPA-I</u>

Following Heald and Speight [14] and Woo [4], the absorption efficiency of dislocations in the case of SIPA-I creep is given by:

$$z_j^n(\sigma) = z_j^0 \left[1 - \frac{z_0^j \sigma}{2\pi\mu e_j^0} \left(Q_j^n + \Delta Q_j \cos^2 \varphi_n \right) \right], \tag{4.15}$$

with:

$$Q_j^n = -\frac{\alpha_j^\kappa}{4\Omega\mu} \frac{(1-2\nu)^2}{1-\nu^2} - \frac{\alpha_j^\mu}{6\Omega\mu} \frac{1}{1-\nu} [-(1+\nu) + 3\nu \cos^2 \theta_n], \tag{4.16}$$

$$\Delta Q_j = -\frac{\alpha_j^\mu}{2\Omega\mu(1-\nu)}, \tag{4.17}$$

where e_j^0 is relaxation strain within the point defect j in the absence of an applied field σ, and α_j^κ and α_j^μ are factors depending on the point defect elastic polarizabilities. The factor 2π in the Eq. 18 was omitted in Ref. [4].

The relaxation strain e_j^0 is related to the relaxation volume ΔV_j through:

$$e_j^0 = \frac{1+\nu}{3(1-\nu)} \frac{\Delta V_j}{\Omega}. \tag{4.18}$$

The factors α_j^κ et α_j^μ are defined as follows:

$$\alpha_j^\kappa = -\Omega \left(\frac{1}{x_j} \frac{\Delta\kappa^j}{\kappa} \right) \kappa, \tag{4.19}$$

$$\alpha_j^\mu = -\frac{\Omega}{5} \left[2 \left(\frac{1}{x_j} \frac{\Delta c_j'}{c'} \right) c' + 3 \left(\frac{1}{x_j} \frac{\Delta C_{44}^j}{C_{44}} \right) C_{44} \right], \tag{4.20}$$

with $c' = (C_{11} - C_{12})/2$, $\left(\frac{1}{x_j} \frac{\Delta\kappa^j}{\kappa} \right)$, $\left(\frac{1}{x_j} \frac{\Delta c_j'}{c'} \right)$ and $\left(\frac{1}{x_j} \frac{\Delta C_{44}^j}{C_{44}} \right)$ the point defect elastic polarizabilities, and x_j the atomic concentration of point defects. In this work, the vacancy polarizabilities are taken equal to zero.

The dislocation sink strength $k_{j,d}^2$ in the case of SIPA-I is given by:

$$k_{j,d}^2 = \sum_n \rho_n z_j^n = \rho_D z_j^0 \left[1 - \frac{z_0^j \sigma}{2\pi\mu e_j^0} \left(\overline{Q_j} + \Delta Q_j \sum_n f_n \cos^2 \varphi_n \right) \right]. \tag{4.21}$$

where f_n is the fraction of dislocations of class n ($\rho_n = f_n \rho_D$), $\overline{Q_j}$ is the average value of Q_j^n (we neglect here the variation of the line direction for the different classes n as in Ref. [4]).

Dislocation sink strength in the case of SIPA-AD

Following Ref. [6], for a uniaxial stress σ the absorption efficiency of dislocations in the case of SIPA-AD creep is given by:

$$z_j^n(\sigma) = z_j^0\left[1 + q^j \cos^2\theta_n\right], \tag{4.22}$$

$$q^j = \frac{3}{8}\frac{P^j}{k_B T}\left(1 - p_1^j\right)\frac{\sigma}{\mu}. \tag{4.23}$$

where $\boldsymbol{P}_j^{SP}$ is the elastic dipole tensor of the point defect j at saddle point, $P^j = \frac{1}{3}\mathrm{tr}\left(\boldsymbol{P}_j^{SP}\right)$, and p_i^j are normalized eigenvalues of $\boldsymbol{P}_j^{SP}$ (so that $\sum_{i=1}^{3} p_i^j = 3$). p_1^j is the normalized eigenvalue whose eigenvector is along the jump direction (Cf. Table 5).

The dislocation sink strength $k_{j,d}^2$ for the j^{th} kind of point defect is given by

$$k_{j,d}^2 = \sum_n \rho_n z_j^n = \rho_D z_j^0\left[1 + q^j \sum_n f_n \cos^2\theta_n\right]. \tag{4.24}$$

Foil surface sink strength

The foil surface sink strength can be written, knowing the sample thickness $2l$ [13]:

$$k_{j,s}^2 = \frac{\sqrt{z_j^0\rho_d}}{l}\left[\coth\left(l\sqrt{z_j^0\rho_d}\right) - \frac{1}{\sqrt{z_j^0\rho_d}\,l}\right]^{-1}. \tag{4.25}$$

Estimation of the pinning point lifetimes

The pinning lifetimes as a function of the stress level are estimated and represented in Figure 9 for a dislocation density of 10^{13} m^{-2}. For the SIPA mechanisms two configurations are considered: if the sinks are only the edge dislocations (i.e. $k_j^2 = k_{j,d}^2$) or if the free surfaces sink strength is also taken into account (i.e. $k_j^2 = k_{j,d}^2 + k_{j,s}^2$).

In the case of climb and glide induced by dislocation bias, as mentioned earlier, the pinning lifetime does not depend on stress (in blue in Figure 9). In the conditions of the experiments, the pinning lifetime is around 1.35×10^3 s, which is more than 30 times larger than found in the experiments.

As expected [6], if the only sinks are the edge dislocations, SIPA-AD (in green in Figure 9) prevails over SIPA-I (in red in Figure 9) (lower lifetime for SIPA-AD than for SIPA-I), and the lifetimes for both mechanisms decrease with stress. In the conditions of the experiments, SIPA-I and SIPA-AD (without surfaces) respectively predict a pinning lifetime of 9.69×10^4 s and 5.81×10^3 s, which is more than 2400 and 140 times larger than in the experiments.

If the surfaces are taken into account in the two SIPA models, the pinning lifetimes become on the same order of magnitude as for the climb and glide induced by dislocation bias model. Yet, they both weakly vary with stress. For the SIPA-I mechanism, the lifetime decreases slightly with stress, whereas for the SIPA-AD mechanism it first remains almost constant then it decreases at very high stresses (over 875 MPa for a dislocation density of 10^{13} m^{-2}) as shown in Figure 9. This weak decrease of the pinning lifetime with stress for both SIPA mechanisms is due to the fact that, as stated earlier, the free surfaces sink strength dominates the dislocation sink strengths. For SIPA-AD in particular, up to very high stresses, the climb velocity is maximum for the two classes of dislocations whose velocity depends very weakly on stress through the term $D_j C_j$ (i.e. $n = 2$ and $n = 3$). Then, at very high stresses, the climb velocity is maximum for the first dislocation class (whose dependence on stress comes from z_j^n and $D_j C_j$). This explains the change in slope at 875 MPa shown by the black arrows in Figure 9.

In the conditions of the experiments, for both SIPA models with surfaces, the pinning lifetime is over 1.3×10^3 s, as in the case of climb and glide induced by dislocation bias. Therefore, not only do these mechanisms predict pinning lifetimes at least one order of magnitude higher than in the experiments, but they also do not show the same sensitivity to stress as in the experiments.

The models used here are quite simple mean field models. Using more advanced models, considering for instance the dislocation positions with respect to the surfaces, could lead to different values of climb velocities and pinning lifetimes. However, it is unlikely that such more complex models will increase the climb velocities by a factor of 30.

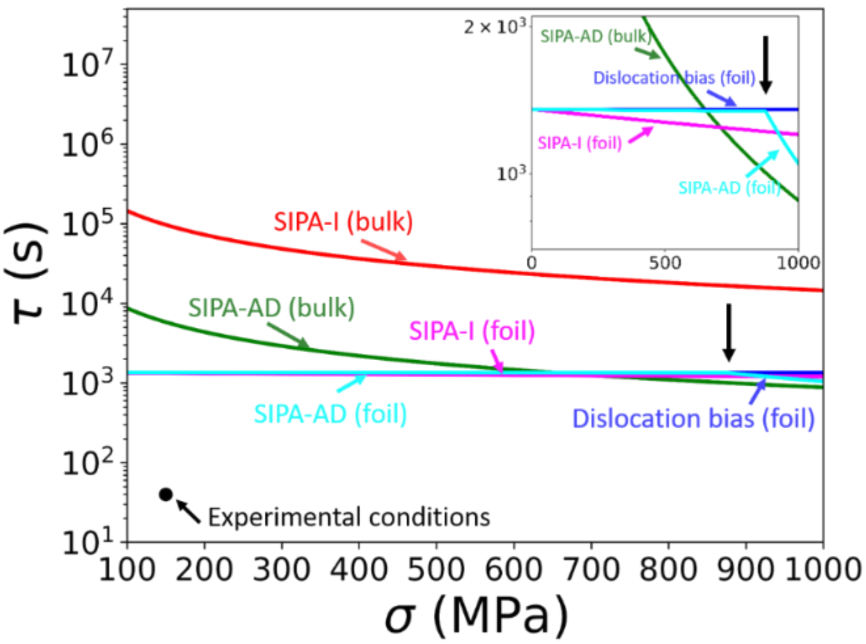

Figure 9 – Evolution of the pinning lifetime with the stress for climb driven by dislocation bias, and SIPA mechanisms (with and without taking into account the foil surfaces strengths). The black point represents the experimental conditions, and the black arrows point to the transition between a regime where the pinning lifetime does not depend on stress and a regime where it depends on stress for SIPA-AD with surfaces.

References

[1] J. Schindelin, I. Arganda-Carreras, E. Frise, V. Kaynig, M. Longair, T. Pietzsch, S. Preibisch, C. Rueden, S. Saalfeld, B. Schmid and J. Tinevez, "Fiji: an open-source platform for biological-image analysis," *Nature methods,* vol. 9, no. 7, pp. 676-682, 2012.

[2] H. Bethe and J. Ashkin, Experimental nuclear physics., New York: Wiley, 1953.

[3] K. Urban, " Radiation-induced processes in experiments carried out in-situ in the high-voltage electron microscope.," *Physica Status Solidi. A, Applied Research,* vol. 56, no. 1, pp. 157-168, 1979.

[4] C. H. Woo, "Effects of an anisotropic dislocation structure on irradiation creep due to stress induced preferred absorption of point defects," *Journal of Nuclear Materials,* vol. 80, no. 1, pp. 132-143, 1979.

[5] R. Bullough and J. R. Willis, "The stress-induced point defect-dislocation interaction and its relevance to irradiation creep," *Philosophical Magazine,* vol. 31, no. 4, pp. 855-861, 1975.

[6] C. H. Woo, "Irradiation creep due to elastodiffusion," *Journal of Nuclear Materials,* vol. 120, no. 1, pp. 55-64, 1984.

[7] H. B. Huntington, "The elastic constants of crystals," *Solid state physics,* vol. 7, pp. 213-351, 1958.

[8] P. H. Dederichs, C. Lehmann and A. Scholz, "Change of elastic constants due to interstitials," *Zeitschrift für Physik B Condensed Matter,* vol. 20, no. 2, pp. 155-163, 1975.

[9] P. Ehrhart, P. Jung, H. Schultz and H. Ullmaier, "Atomic Defects in Metals," in *Landolt-Börnstein, New Series, Group III/25*, H. Ullmaier. Springer-Verlag, 1991.

[10] C. Padovani, D. Pletser, K. Jurkschat, D. Armstrong, S. Dugdale, D. Brunt, R. Faulkner, G. Was and A. J. Johansson, Assessment of microstructural changes in copper due to gamma radiation damage., SKB TR-19-12, Svensk Kärnbränslehantering AB., 2019.

[11] A. Vattré, T. Jourdan, H. Ding, M. C. Marinica and M. J. Demkowicz, "Non-random walk diffusion enhances the sink strength of semicoherent interfaces.," *Nature communications,* vol. 7, no. 1, pp. 1-10, 2016.

[12] G. Was, Fundamentals of radiation materials science: metals and alloys, Springer, 2016.

[13] R. Bullough, M. R. Hayns and M. H. Wood, "Sink strengths for thin film surfaces and grain boundaries," *Journal of Nuclear Materials,* vol. 90, no. 1-3, pp. 44-59, 1980.

[14] P. T. Heald and M. V. Speight, " Point defect behaviour in irradiated materials," *Acta Metallurgica,* vol. 23, no. 11, pp. 1389-1399, 1975.